Electronic Supplementary Information (ESI)

Diffusion driven nanostructuring of metal–organic frameworks (MOFs) for graphene hydrogel based tunable heterostructures: highly active electrocatalysts for efficient water oxidation

Anirban Sikdar[a], Abhisek Majumdar[a], Abhijit Gogoi[b], Pronoy Dutta[a], Munu Borah[a], Soumen Maiti[c], Chiranjib Gogoi[d], K. Anki Reddy[e,], Youngtak Oh[f,*], Uday Narayan Maiti[a,*]*

[a]Department of Physics, Indian Institute of Technology Guwahati, Guwahati-781039, Assam, India

E-mail: udaymaiti@iitg.ac.in

[b]Department of Mechanical Engineering, Indian Institute of Technology Guwahati, Guwahati-781039, Assam, India

[c]St. Thomas College of Engineering & Technology, Kolkata, 700032, India

[d]Department of Chemistry, Indian Institute of Technology Guwahati, Guwahati-781039, Assam, India

[e]Department of Chemical Engineering, Indian Institute of Technology Guwahati, Guwahati-781039, Assam, India

E-mail: anki.reddy@iitg.ac.in

[f]Center for Environment, Health, and Welfare Research, Korea Institute of Science and Technology, Seoul 02792, Republic of Korea

E-mail: ytoh@kist.re.kr

1. Experimental section:

1.1. Materials:

Graphite powder, nickel acetate (II) tetrahydrate ($Ni(CH_3COO)_2.4H_2O$), cobalt (II) nitrate hexahydrate ($Co(NO_3)_2.6H_2O$), cobalt (II) acetate tetrahydrate ($Co(CH_3COO)_2.4H_2O$), iron (III) nitrate nonahydrate ($Fe(NO_3)_3.9H_2O$), iron (II) acetate ($Fe(CH_3COO)_2$), 2-methyl imidazole (2-mIm), terephthalic acid (BDC), trimesic acid (BTC), aniline, dimethyl sulfoxide (DMSO), 1-octanol, chloroplatinic acid (H_2PtCl_6), sodium borohydride ($NaBH_4$), 5 wt% nafion, ruthenium oxide (RuO_2) were purchased from Sigma-Aldrich. Zinc (III) nitrate hexahydrate ($Zn(NO_3)_2.6H_2O$), ammonium peroxydisulfate ($(NH_4)_2S_2O_8$), potassium hydroxide (KOH) pellets, ethanol, hydrochloric acid (HCl) were purchased from Merck. Zn plate, copper acetate monohydrate ($Cu(COOCH_3)_2.H_2O$), 35% ammonium hydroxide solution (NH_4OH), chloroform were provided by Alfa Aesar. A Millipore type III deionized water (DI water) was used in all the experiments. All the reagents were used without any further purification.

1.2. Preparation of porous graphene hydrogel (PG):

The PG was prepared following our previous synthetic strategy of electroless reduction of graphene oxide with some modifications.[1, 2] An aqueous dispersion of 4 mg/mL graphene oxide solution (20 mL) was first mixed with an equal volume (1:1 V/V) of NH_4OH. Then a polished zinc plate (Zn) was put directly into the graphene oxide-NH_4OH solution for 5 min. Subsequently, film of PG developed over Zn was washed thoroughly with water and the PG was detached from Zn surface by reacting it with 8 M KOH solution. Finally the PG was washed with water to remove KOH and kept in water for further use.

1.3. General synthetic strategy for various nanomaterial-PG hybrids:

The as formed PG was hybridized with different nanomaterials via gel-organic interfacial self-assembly method. In all the following reactions the embedded water of PG was first saturated with respective aqueous phase for 24 hours. Subsequently PG saturated with aqueous phase was immersed in organic solution of respective reactants to start the interfacial reaction for another 24 hours. Finally the PG nanohybrids were taken out of the organic phase and washed with ethanol, water repeatedly to remove any impurities. Following this protocol we have developed various PG based hybrids e.g. MOF-PG ($_{AOG}$Cu(BTC)-PG, $_{AOG}$ZIF67-PG, $_{AOG}$ZIF8-PG, $_{AOG}$TM-PG[S], $_{AOG}$TM-PG[R]), conducting polymer (PANI)-PG ($_{AOG}$PANI-PG) and metal nanoparticles-PG ($_{AOG}$Pt-PG).

1.3.1. Detailed synthesis of various MOF-PG nanohybrids: For the interfacial synthesis of $_{AOG}$ZIF67-PG, the aqueous phase was prepared by $Co(NO_3)_2.6H_2O$ (0.137 M) dissolved in DI water and the corresponding organic solution was prepared by dissolving 2-mIm (0.61 M) in $CHCl_3$. In case of $_{AOG}$ZIF8-PG, the aqueous solution was made by $Zn(NO_3)_2.6H_2O$ (0.098 M) dissolved in D.I water and the organic phase was prepared by 2-mIm (0.394 M) dissolved in $CHCl_3$. In case of $_{AOG}$Cu(BTC)-PG, aqueous phase contained $Cu(COOCH_3)_2.H_2O$ (0.36 M) in DI water while BTC (0.08 M) dissolved in 1-octanol served as the organic phase. For the synthesis of tri-metallic $_{AOG}$TM-PG[R] hybrids, the aqueous phase was prepared by dissolving $Ni(CH_3COO)_2.4H_2O$ (0.123 M), $Co(CH_3COO)_2.4H_2O$ (0.061 M) and $Fe(NO_3)_3.9H_2O$ (0.015 M) in D.I water. The corresponding organic phase was prepared by first dissolving BDC (0.2 M) in a mixed solvent of 1-octanol and DMSO (3:2 v/v). For, the synthesis of $_{AOG}$TM-PG[S], all the reactant concentrations remained same as in the case of $_{AOG}$TM-PG[R], except instead of $Fe(NO_3)_3.9H_2O$, $Fe(CH_3COO)_2$ (0.015 M) was used. The reaction conditions stated above are the primary conditions to synthesize MOF-PG hybrids via hydrogel-organic interfacial reaction.

In order to study the effect of concentration of reactants on the morphology of the samples two other concentrations of reactants were taken as tabulated below.

Table S1: Concentration variation of various MOF-PG hybrids.

Material	Other concentrations 1	Other concentrations 2
AOGZIF67-PG	$Co(NO_3)_2.6H_2O$- 0.0685 M 2-mIm- 0.305 M	$Co(NO_3)_2.6H_2O$- 0.274 M 2-mIm- 1.22 M
AOGZIF8-PG	$Zn(NO_3)_2.6H_2O$- 0.049 M 2-mIm- 0.197 M	$Zn(NO_3)_2.6H_2O$- 0.196 M 2-mIm- 0.788 M
AOGCu(BTC)-PG	$Cu(COOCH_3)_2.H_2O$- 0.09 M BTC- 0.02 M	$Cu(COOCH_3)_2.H_2O$- 0.18 M BTC- 0.04 M
AOGTM-PG[R]	$Ni(CH_3COO)_2.4H_2O$- 0.062 M $Co(CH_3COO)_2.4H_2O$- 0.031 M $Fe(NO_3)_3.9H_2O$- 0.0075 M BDC- 0.1 M	$Ni(CH_3COO)_2.4H_2O$- 0.248 M $Co(CH_3COO)_2.4H_2O$- 0.124 M $Fe(NO_3)_3.9H_2O$- 0.03 M BDC- 0.4 M
AOGTM-PG[S]	$Ni(CH_3COO)_2.4H_2O$- 0.062 M $Co(CH_3COO)_2.4H_2O$- 0.031 M $Fe(CH_3COO)_2$- 0.0075 M BDC- 0.1 M	$Ni(CH_3COO)_2.4H_2O$- 0.248 M $Co(CH_3COO)_2.4H_2O$- 0.124 M $Fe(CH_3COO)_2$- 0.03 M BDC- 0.4 M

Depending upon the reactant concentrations we named our samples where necessary, as AOGMOF-PGHigh, AOGMOF-PGMed and AOGMOF-PGLow for highest, moderate and low concentrations of reactants.

1.3.2. Synthesis of PANI-PG nanohybrids: AOGPANI-PG nanohybrids were synthesized according to the previously reported method with some modification.[3] During the synthesis of

PANI nanowires within PG, the water phase was prepared by dissolving $(NH_4)_2S_2O_8$ (0.8 M) in HCl (1 M) and the organic phase was made by dissolving aniline (0.32 M) in $CHCl_3$.

1.3.3. Synthesis of noble metal (Pt)-PG nanohybrids: For the diffusion controlled interfacial synthesis of $_{AOG}$Pt-PG hybrid, the aqueous phase was constructed by $NaBH_4$ (0.042 M) dissolved in D.I water and the corresponding organic phase consisted of H_2PtCl_6 (0.0029 M) dispersed in chloroform.

1.4. Controlled bulk phase interfacial synthesis of MOF nanoparticles without PG:

In a typical bulk phase interfacial synthesis of MOFs ($_{AO}$Cu(BTC), $_{AO}$ZIF67, $_{AO}$ZIF8 and $_{AO}$TM[R]), the concentration of reactants remained the same as described above, except without saturating PG with aqueous phase, the aqueous solutions of the respective metal precursors were slowly put directly over the top of the corresponding organic phases. After a reaction of 24 hours, the MOFs synthesized at the interface were collected and centrifuged repeatedly with ethanol and water in order to remove any unreacted reactants. Finally the MOFs were dried in vacuum for 24 hrs.

1.5. Bulk water phase synthesis of MOFs:

For the bulk water phase synthesis of $_A$Cu(BTC), $_A$ZIF67 and $_A$ZIF8 and $_A$TM[R] MOFs the metal and ligand concentrations remained the same as in the case of interfacial method (section 1.3.1) except the ligands were dispersed in D.I water. Only in case of $_A$Cu(BTC) and $_A$TM[R], due to poor solubility of BTC/BDC in water, it was dissolved in DMSO with the same concentration as previously stated.

1.6. Controlled water phase synthesis of MOF-PG hybrids:

For the aqueous phase synthesis of $_{AG}$Cu(BTC)-PG, $_{AG}$ZIF67-PG and $_{AG}$ZIF8-PG, the PG was first saturated with respective aqueous phase with the same metal ion concentration as

mentioned in the case of interfacial reaction (section 1.3.1). Next the gel containing metal ions were put in the aqueous solution of respective ligand molecules. Except in the case of $_{AG}Cu(BTC)$-PG, due to poor solubility of BTC in water, the PG containing copper solution was put in a solution of BTC dissolved in DMSO.

1.7. Material characterization:

The morphology of the as synthesized materials were characterized with Zeiss Sigma 300 FE-SEM. A JEOL 2100F FE-TEM operated at 200 kV was used to study the morphology, lattice fringes and elemental mapping (STEM). The crystal structure of various samples were examined in powder XRD mode using Rigaku X-ray diffractometer. The energy dispersive X-ray spectroscopic (EDAX) analysis was performed using Ametek EDAX module attached to FE-SEM. For ionic state and the elemental analysis, XPS was carried out in ESCALAB Xi+ (Thermo Fisher) instrument. N_2 sorption isotherms were recorded by using Quantachrome Quadrasorb evo surface area (Brunauer–Emmett–Teller, BET) analyser at 77K. Before the sorption analysis, the degassing of the samples were carried out at 100°C under high vacuum for 12 h.

1.8. Electrochemical measurements:

All the electrochemical measurements were performed at room temperature in a standard three-electrode cell configuration with as synthesized MOF-PG hybrid deposited over nickel foam as the working electrode, a platinum wire (CHI) as counter electrode and a saturated calomel electrode (SCE) (CHI 150) as reference electrode. A PARSTAT 3000A-DX potentiostat controlled by Versa Studio software was used for the electrochemical characterizations. For the preparation of working electrode, 3 mg of freeze dried MOF-PG hybrid or RuO_2 catalyst was dispersed in 3 mL absolute ethanol (Merck, Empsure) by sonication. After forming a uniform suspension, 40 µL of 5 wt% Nafion was added to it and the suspension was further

sonicated for 20 min. to form a homogeneous ink. Subsequently the as prepared catalyst ink was drop casted over a pre-cleaned Ni-foam and dried overnight. The final loading of the catalyst was kept fixed at 0.64 mg cm^{-2} for all the samples. The linear sweep voltammetry (LSV) curves were taken in a nitrogen saturated 1 M KOH electrolyte at a scan rate of 5 mV s^{-1} and were corrected with 100% iR drop compensation. All the potentials used in this work were referenced against reversible hydrogen electrode (RHE) according to the formula: $E_{RHE} = E_{SCE} + 0.059 \, pH + 0.242$. The measured current was normalized with geometrical area of the working electrode (1 cm^{-2}). The OER overpotential (η) was calculated following the formula: $\eta = E_{RHE} - 1.23 \, V$. The impedance curves were obtained at the overpotential of 288 mV vs RHE within a frequency range of 0.1 Hz to 10^6 Hz with an AC amplitude of 10 mV.

2. Calculation of various performance metrics:

2.1. Calculation of mass activity:

The mass activity of the catalysts were calculated by normalizing current density (J) at an overpotential of 300 mV by the catalyst mass loading (m) of the electrode:

$$\text{Mass activity} = {J}/{m}$$

2.2. Calculation of double layer specific capacitance (C_{dl}) and estimation of electrochemically active surface area (ECSA):

The double layer capacitance was measured from the cyclic voltammetry (CV) curves obtained within a voltage window of 1.25-1.35 V vs RHE (non Faradaic region) at scan rates of 10-70 mV s^{-1}. The C_{dl} value was obtained from the half of the slope of the $J_a - J_c$ vs v plot; where, J_a and J_c are the anodic and cathodic currents respectively at potential 1.3 V vs RHE and v is the scan rate. The ECSA was estimated to be proportional to the evaluated C_{dl}.

3. Computational methods:

First the structure of all the components (PG, 2-mIm, $Co(NO_3)_2.6H_2O$ and ZIF67) were constructed using Avogadro and VMD.[4, 5] The chemical composition of PG used in this study was $C_{30}O_1(OH)_1(COOH)_{0.5}$ where the epoxy and hydroxyl functional groups were located on the basal plane of the graphene nanosheet and the carboxyl functional groups were located on the edges.[6] All the molecular dynamics (MD) simulations were performed using Nanoscale Molecular Dynamics (NAMD)[7] using all-atom optimized potentials for liquid simulations (OPLS-AA) force field parameters[8] with a time step of 1 fs. The water molecules were modeled using TIP3P water model[9] and their bond length (O-H bond) were constrained using SETTLE algorithm.[10] The van der Waals interactions were computed through Lennard-Jones potential using a cut off distance of 12 Å. The long range electrostatic interactions are computed using Particle mesh Ewald (PME) method.[11] After the equilibration the production runs were performed for 20 ns with NVE ensemble at a temperature of 300.0 K. During the production run the graphene nanosheets at the top and bottom layers were constrained so that at any point of the simulation the boundary of PG layered structure can be accurately defined. However, all other graphene nanosheets and other molecules were allowed to interact with their surroundings freely. Before initiating the MD simulations, energy minimization was performed on the system. Then the system was equilibrated for 1 ns at a temperature of 300.0 K and 1 atm pressure with NPT ensemble. For controlling the pressure, modified Nosé-Hoover method was used where both barostat oscillation time and damping factor were set to 0.3 ps. Temperature was controlled using Langevin dynamics with a damping factor of 5 ps^{-1}. During the equilibration, all the atoms except water, were constrained to their initial positions with a force constraint of 1.0 kcal/ (mol Å^2).
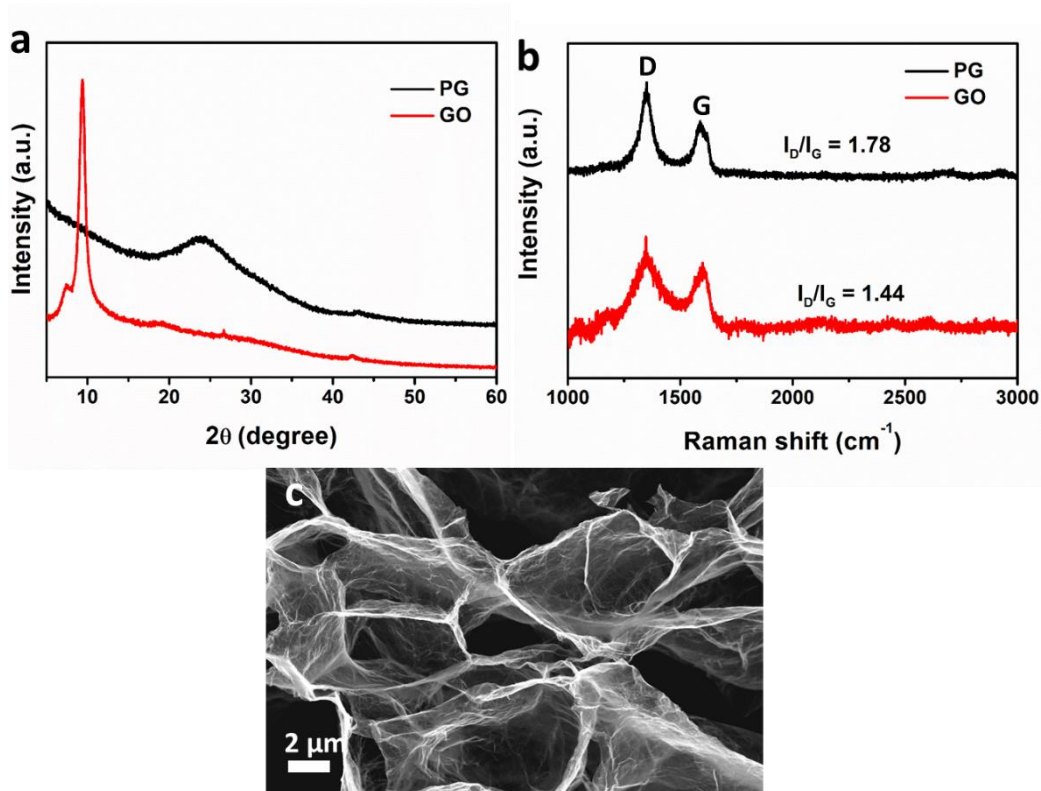
Fig. S1: Characterization of PG: (a) FESEM image of PG; (b) XRD pattern and (c) Raman spectra of GO and PG.

The XRD pattern of GO shows a sharp peak at 2θ of 9.4° corresponding to the (001) plane. After reduction PG exhibits a broad peak at 2θ of 24.1° (d-spacing of 3.7 Å) which corresponds to graphitic (002) plane. The successful reduction of GO into PG is further observed from the Raman spectra where both GO and PG exhibits characteristic D and G bands originating due to the defects and in-plane C=C stretching of graphitic structure respectively. Besides, the intensity ratio of D and G band (I_D/I_G) increases from 1.44 (GO) to 1.78 (PG) due to the increment of sp2 bonded carbon atoms and decrement of sp2 domain size in PG which further confirms the successful reduction process.
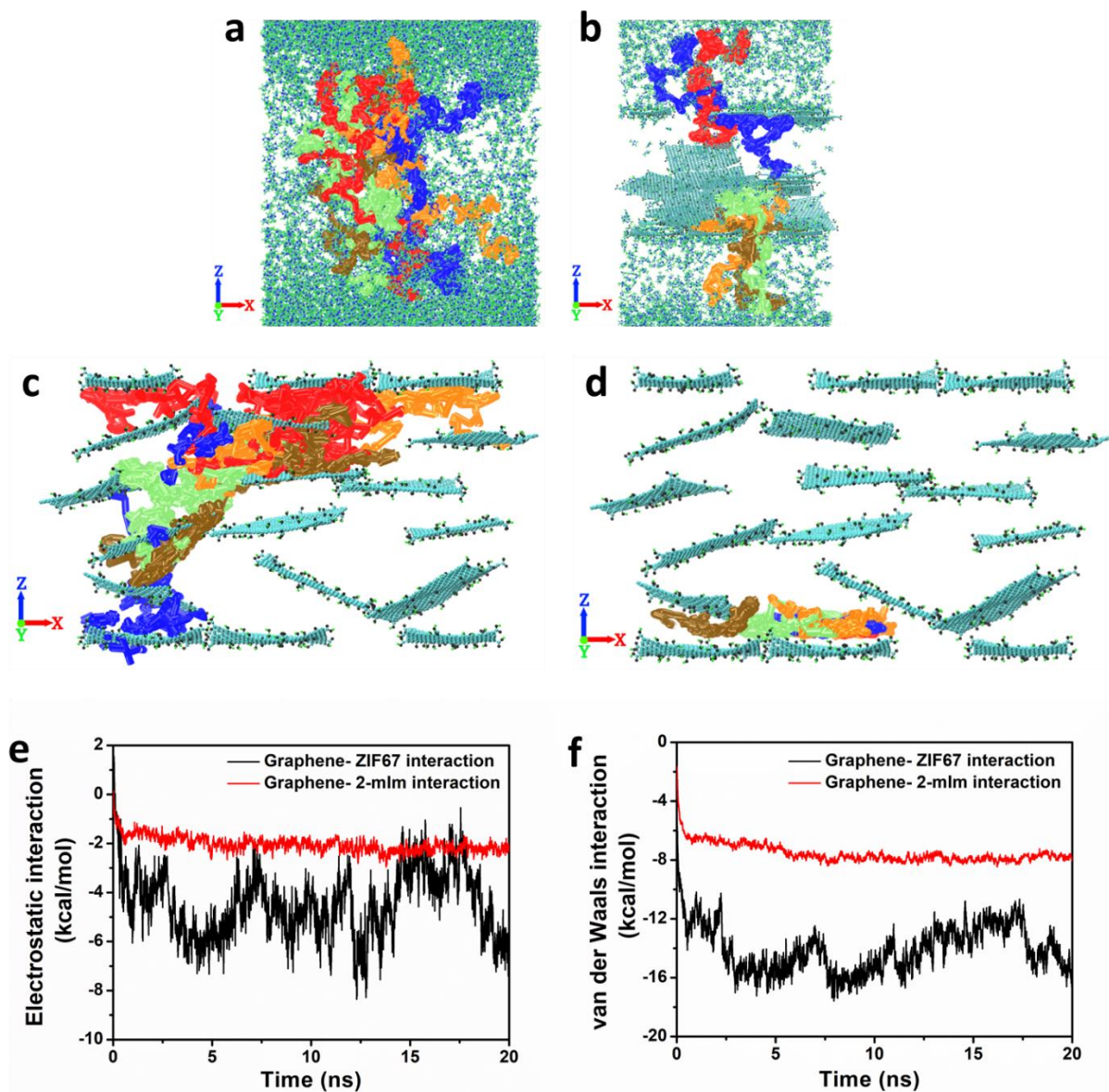
Fig. S2: MD simulation results: (a) representative trajectory of the 2-mIm molecules in the aqueous-organic interface; (b) representative trajectory of the 2-mIm molecules in the graphene hydrogel-organic interface; trajectory of (c) 2-mIm and (d) ZIF67 inside the graphene layers. Trajectory of different 2-mIm/ZIF67 molecules are represented with different colors; (e) electrostatic and (f) van der Waals interaction of ZIF67 and 2-mIm with the basal planes of graphene.

Fig. S1c-d depict the diffusion of 2-mIm is much faster than ZIF67 within the graphene hydrogel. This phenomenon is also evident from the Fig. S1e-f. In these plots, the negative

interaction signifies the attractive interaction. ZIF67 shows stronger electrostatic and van der Waals (vdW) attraction with the graphene as compared to 2-mIm. Comparing these plots (electrostatic and vdW) it is observed that, strong vdW interaction of ZIF67 with graphene nanosheets contributes more in the adsorption of ZIF67 on the basal plane of the graphene nanosheets. These results suggest the possible controlled nucleation and growth of ZIF67 via strong interaction with the graphene sheets.
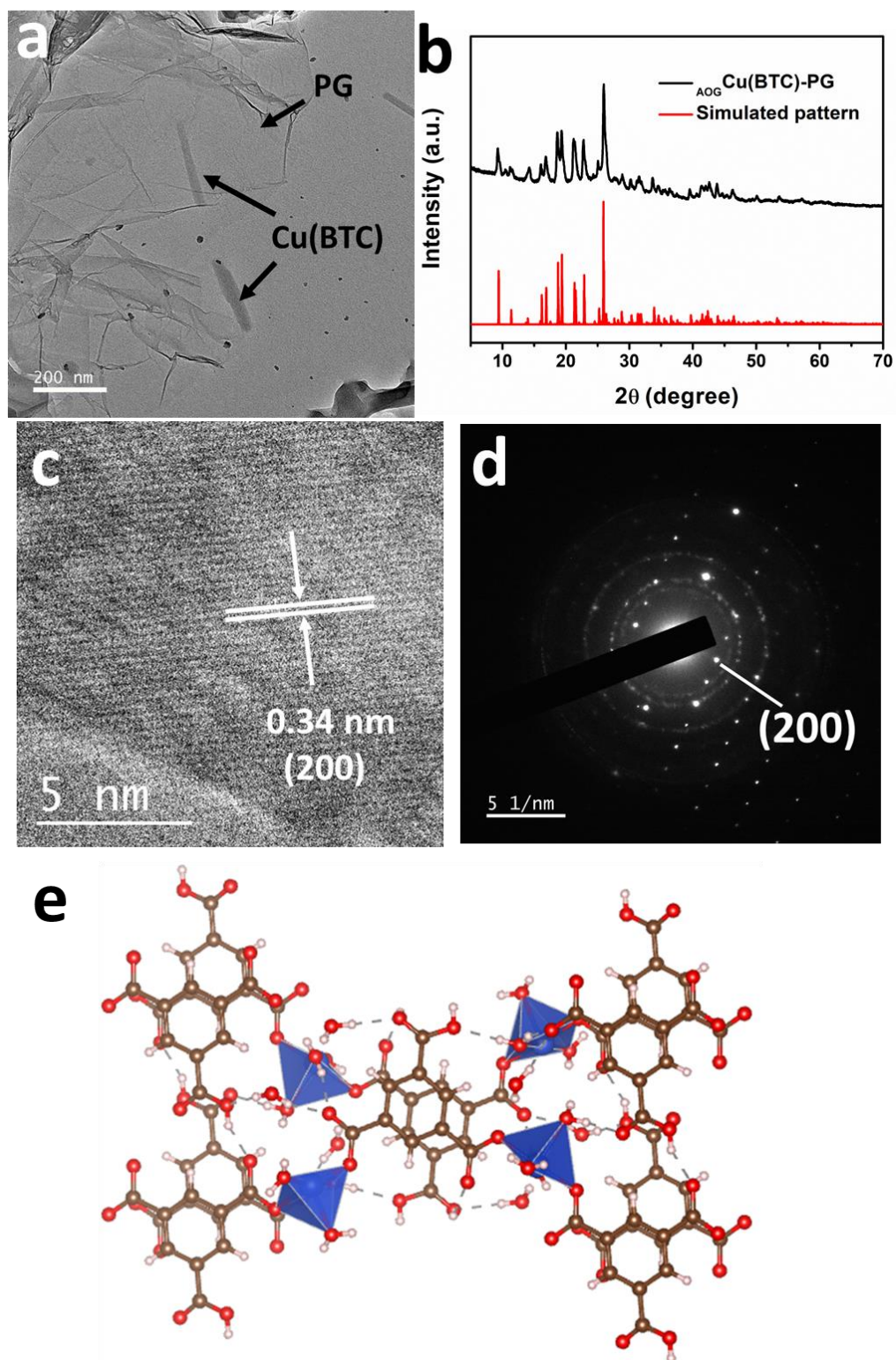
Fig. S3: (a) FE-TEM image, (b) XRD pattern, (c) HR-TEM image and (d) SAED pattern of AOGCu(BTC)-PG. (e) A unit cell of Cu(BTC) crystal in AOGCu(BTC)-PG hybrid. The crystal

structure of $_{AOG}$Cu(BTC) is based on the previously reported Cu(BTC)·3H$_2$O MOF.[12] The simulation of crystal structure is done using VESTA software.

Table S2: Summary of structure determinations of Cu(BTC) of $_{AOG}$Cu(BTC)-PG hybrid.

Material	Cu(BTC)
Crystal system	Monoclinic
Space group	P 2$_{1/c}$
Lattice parameters	
a (Å)	6.87780
b (Å)	18.82060
c (Å)	8.53840
α (˚)	90
β (˚)	92.4710
γ (˚)	90
Volume (Å^3)	1104.2197
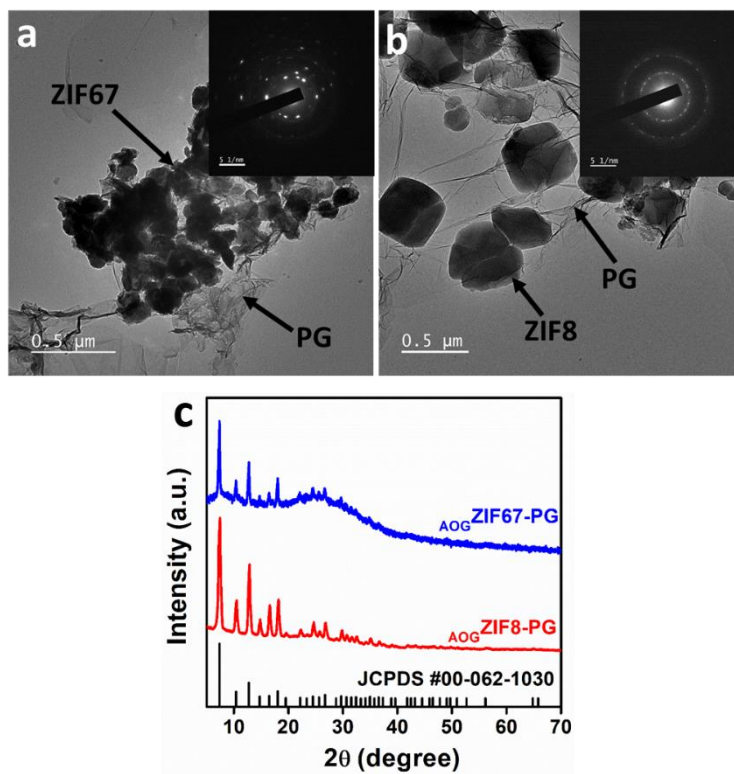
Fig. S4: FE-TEM images of (a) $_{AOG}$ZIF67-PG and (b) $_{AOG}$ZIF8-PG, (c) XRD pattern of $_{AOG}$ZIF67-PG and $_{AOG}$ZIF8-PG. The insets of (a) and (c) show corresponding SAED patterns.
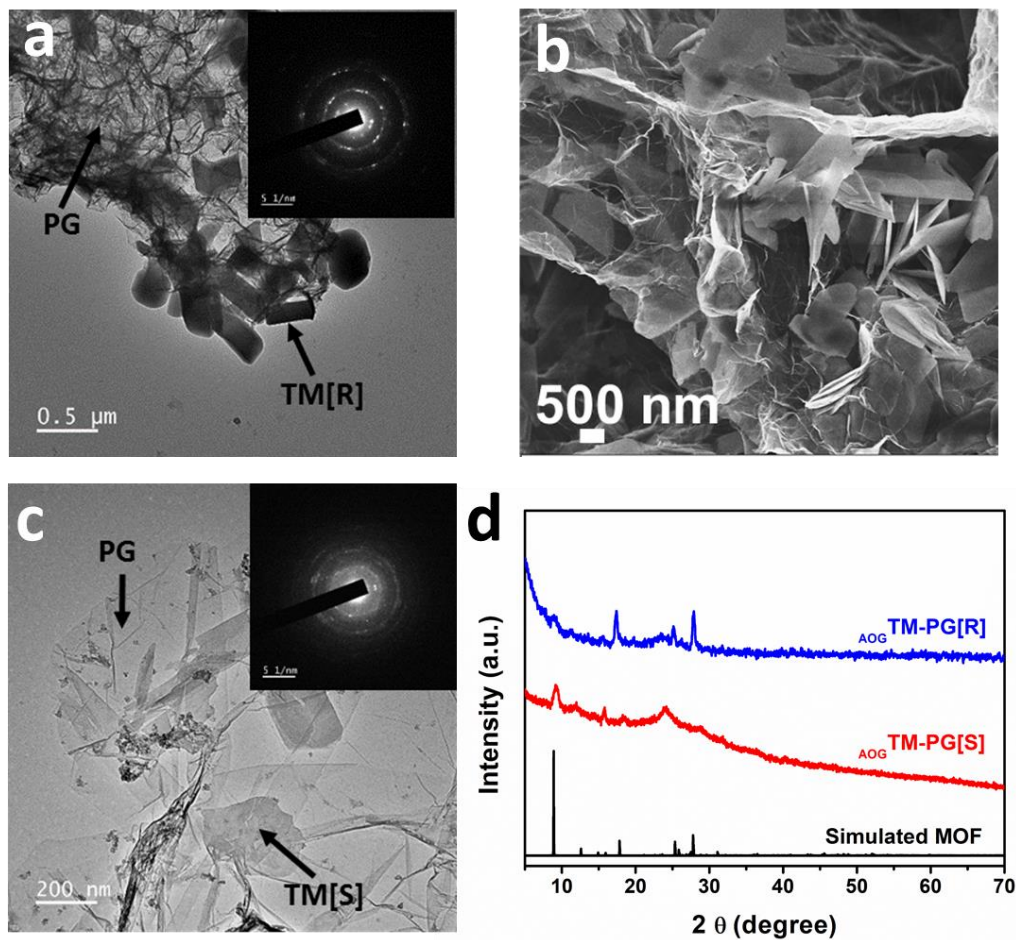
Fig. S5: (a) FE-TEM image of $_{AOG}$TM-PG[R]; (b) FE-SEM and (c) FE-TEM images of $_{AOG}$TM-PG[S] nanohybrids. (TM[R] and TM[S] represent the MOF part of $_{AOG}$TM-PG[R] and $_{AOG}$TM-PG[S] respectively); The insets of (a) and (c) show corresponding SAED patterns; (d) XRD pattern of $_{AOG}$TM-PG[R] and $_{AOG}$TM-PG[S].
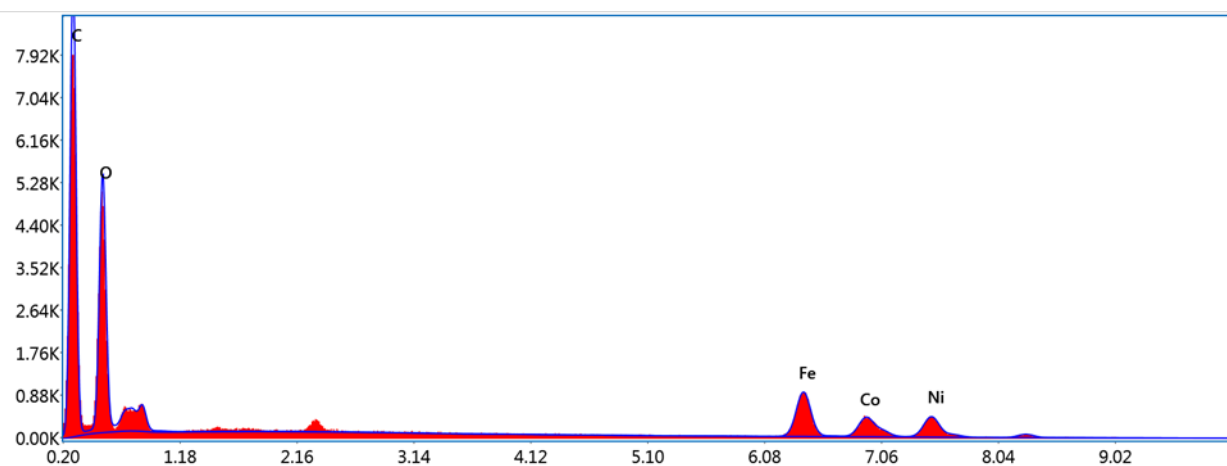
| Element	Weight %	Atomic %	Error %	Net Int.	K Ratio	Z	A	F
C K	46.01	61.78	6.98	2025.34	0.2155	1.0677	0.4386	1.0000
O K	31.70	31.95	9.29	1241.20	0.0764	1.0228	0.2356	1.0000
Fe K	10.20	2.95	3.47	470.09	0.0877	0.7858	1.0161	1.0767
Co K	5.36	1.47	5.04	205.98	0.0437	0.7676	1.0140	1.0458
Ni K	6.73	1.85	4.59	229.43	0.0551	0.7931	1.0035	1.0287

Fig. S6: EDAX elemental analysis of $_{AOG}$TM-PG[R].
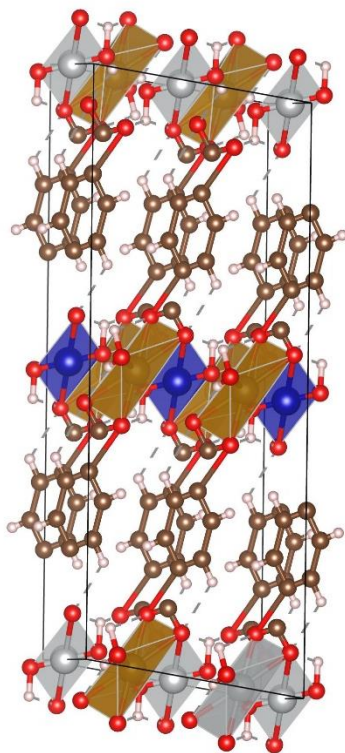
Fig. S7: A unit cell of TM MOF crystal in ₐₒGTM-PG hybrid. The unit cell of ₐₒGTM crystal is constructed using basic Ni-based MOF structure reported previously.[13] The simulation of crystal structure is done using VESTA software following the method reported by Qian et al.[14]

Table S3: Summary of structure determinations of TM of AOGTM-PG hybrid.

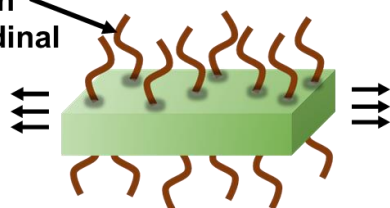| Material	TM
Crystal system	Triclinic
Space group	P1
Lattice parameters	
a (Å)	7.74407
b (Å)	7.80632
c (Å)	20.2100
α (˚)	90.5044
β (˚)	80.5890
γ (˚)	115.5600
Volume (Å^3)	1084.7233
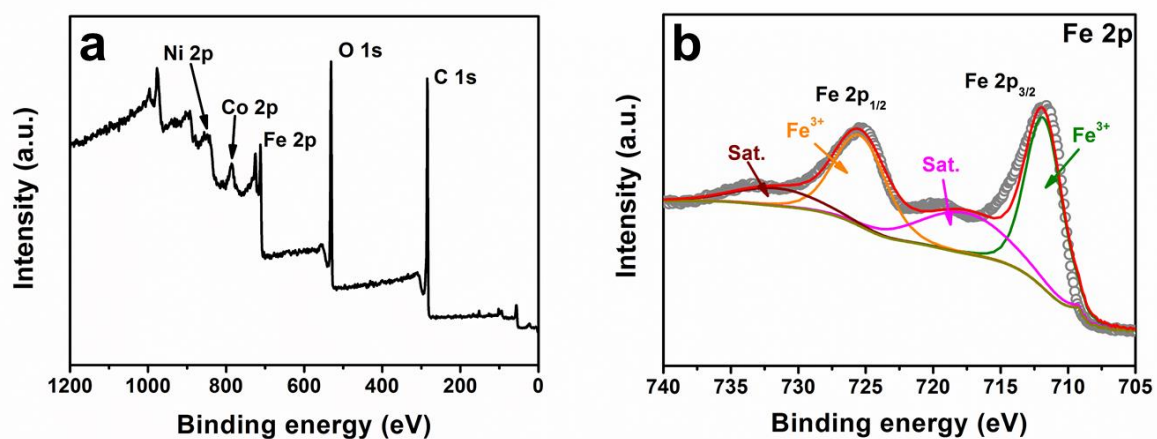
Fig. S8: (a) XPS survey spectrum and (b) Fe 2p spectra of AOGTM-PG[R]

.
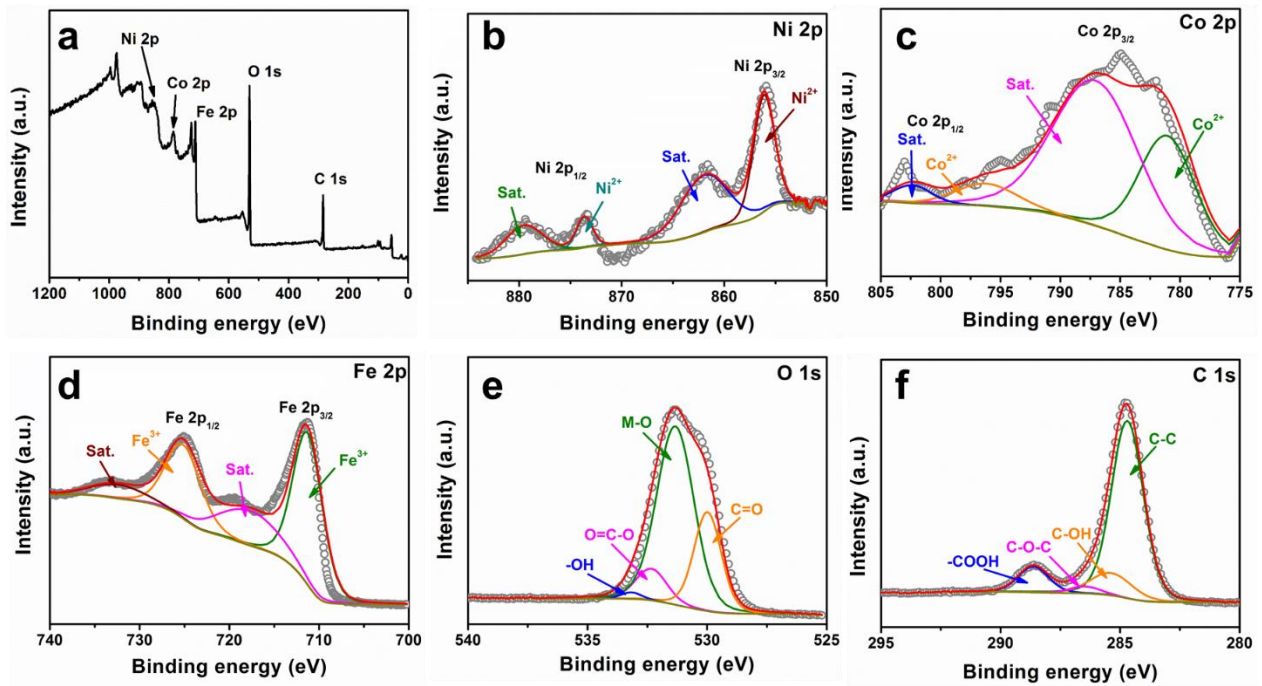
Fig. S9: (a) XPS survey spectrum, (b) Ni 2p, (c) Co 2p, (d) Fe 2p, (e) O 1s and (f) C 1s spectra of $_{AOG}$TM-PG[S].

Scheme-1

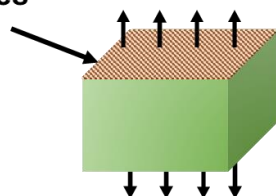**Capping agent inhibits growth along longitudinal direction**

Growth along transverse direction only

Sheet like morphology

Scheme-2

Higher surface energy promotes growth rate

**Higher growth rate along longitudinal direction**

rod like morphology

**Fig. S10:** Growth mechanism of sheet and rod like morphology of MOF nanostructure:

Scheme-1 illustrates the growth mechanism of sheet like morphology of MOF by the capping effect of acetate ions which inhibits the growth rate of caped surface and increases the growth along transverse direction resulting in sheet like morphology. Scheme-2 illustrates the growth of rod like morphology of MOF structure via the difference in surface energy due to effect of graphene sheets which increases the growth rate along the high surface energy faces which gives rise to rod like structure.
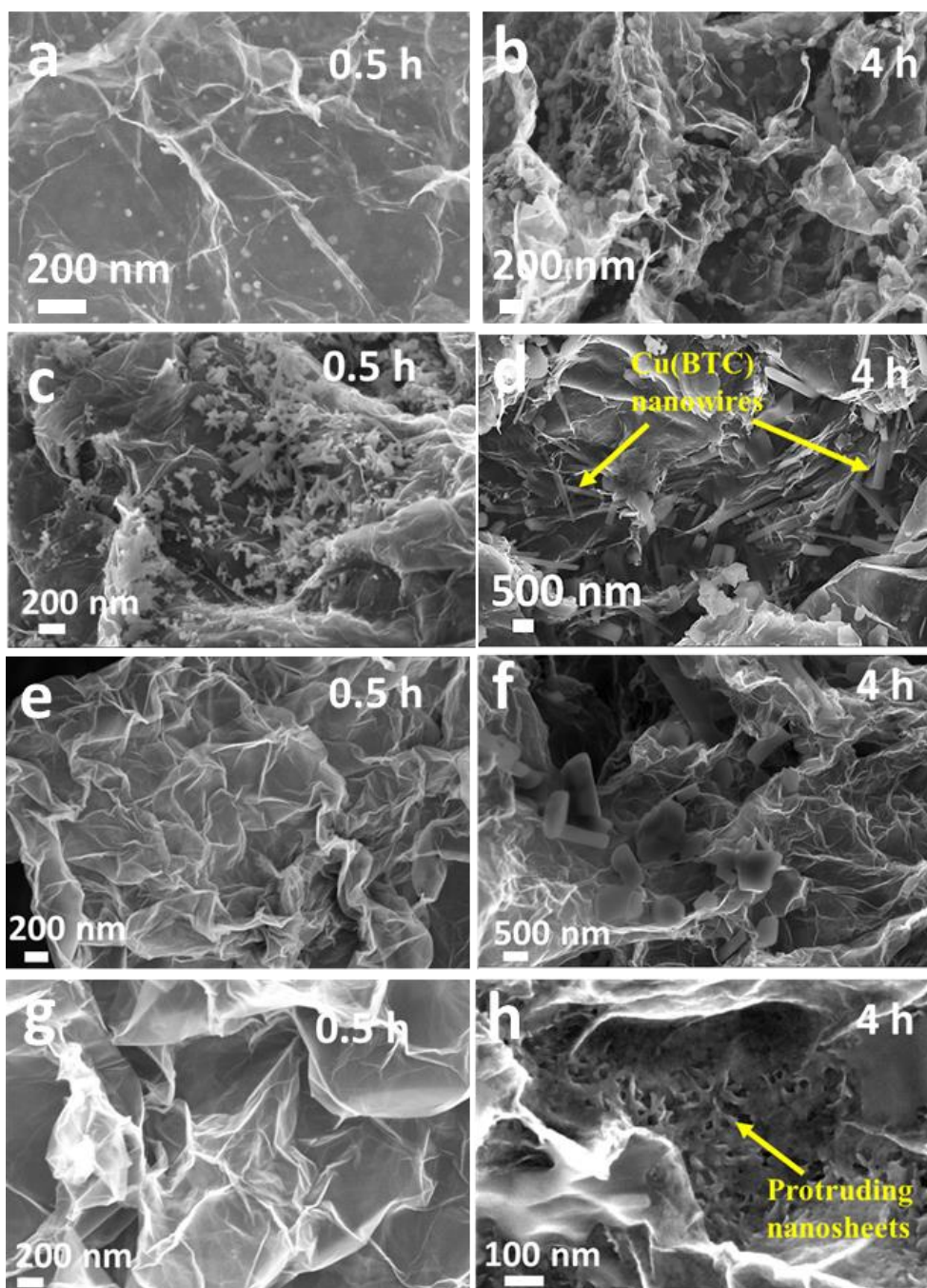
Fig. S11: Time dependent FESEM study for gel-organic interfacial reaction time 0.5 h and 4h: (a)-(b) AOGZIF67-PG, (c)-(d) AOGCu(BTC)-PG, (e)-(f) AOGTM-PG[R] and (g)-(h) AOGTM-PG[S].
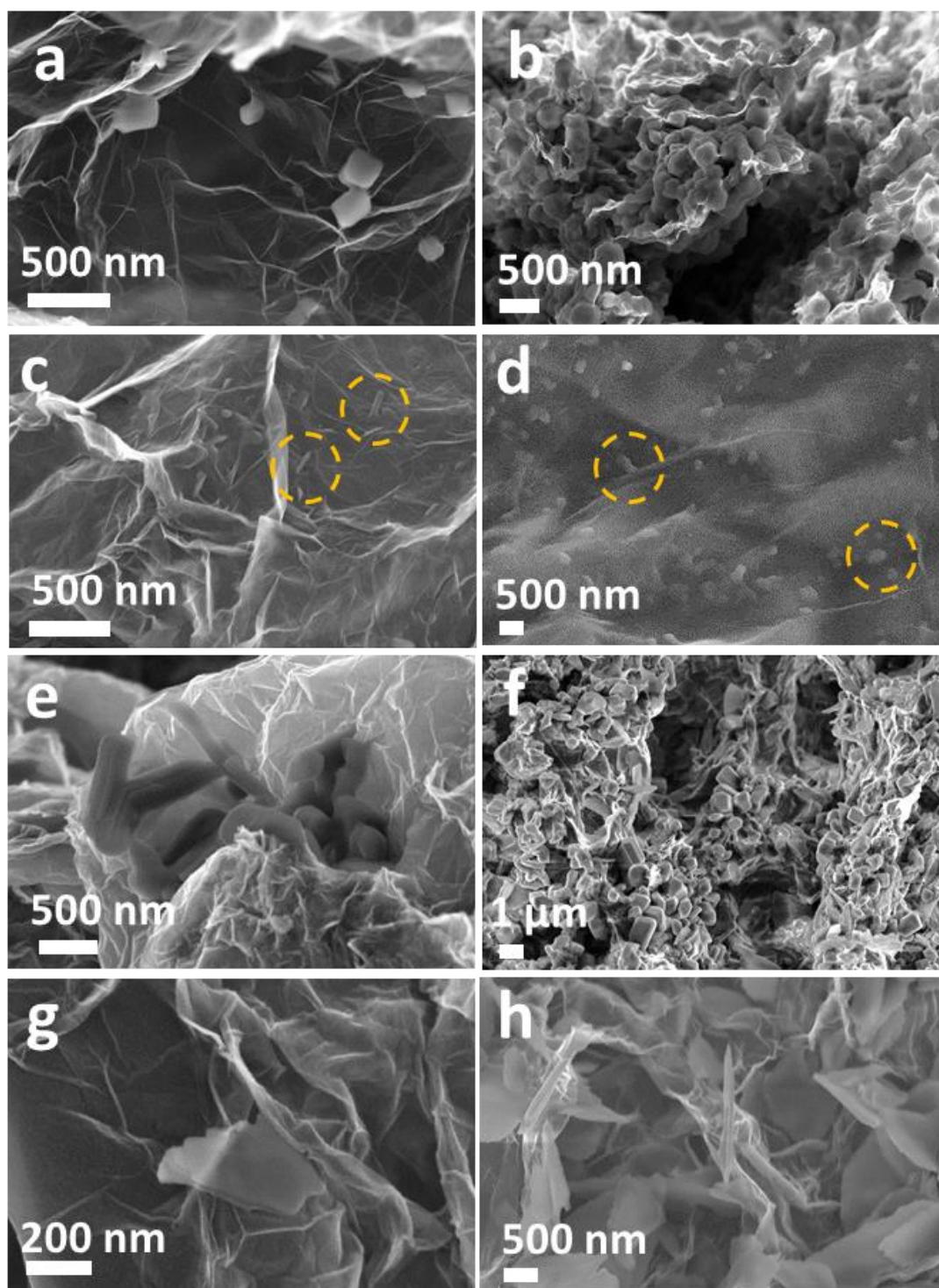
Fig. S12: FE-SEM images of MOFs prepared at different concentrations of reactants: (a)-(b) AOGZIF67-PG, (c)-(d) AOGCu(BTC)-PG, (e)-(f) AOGTM-PG[R] and (g)-(h) AOGTM-PG[S].
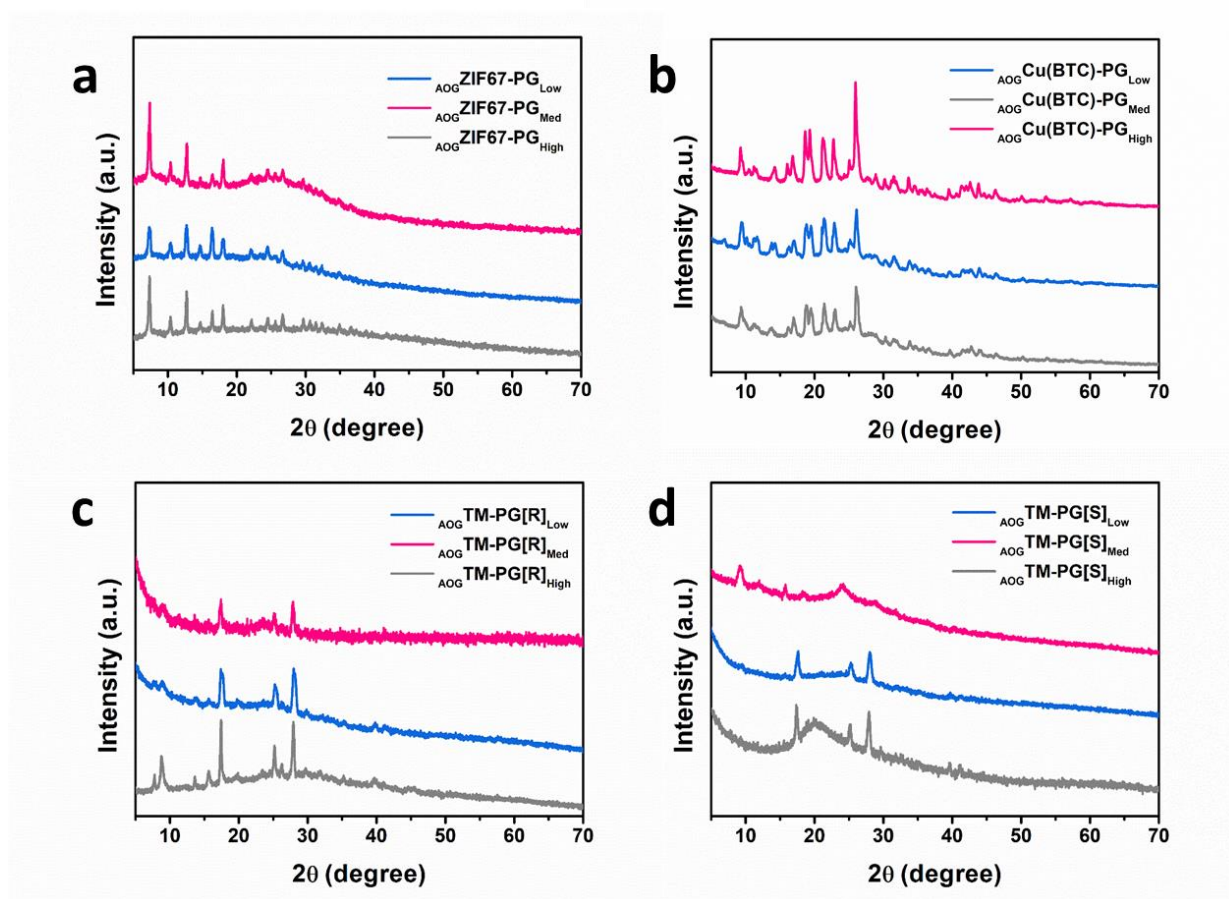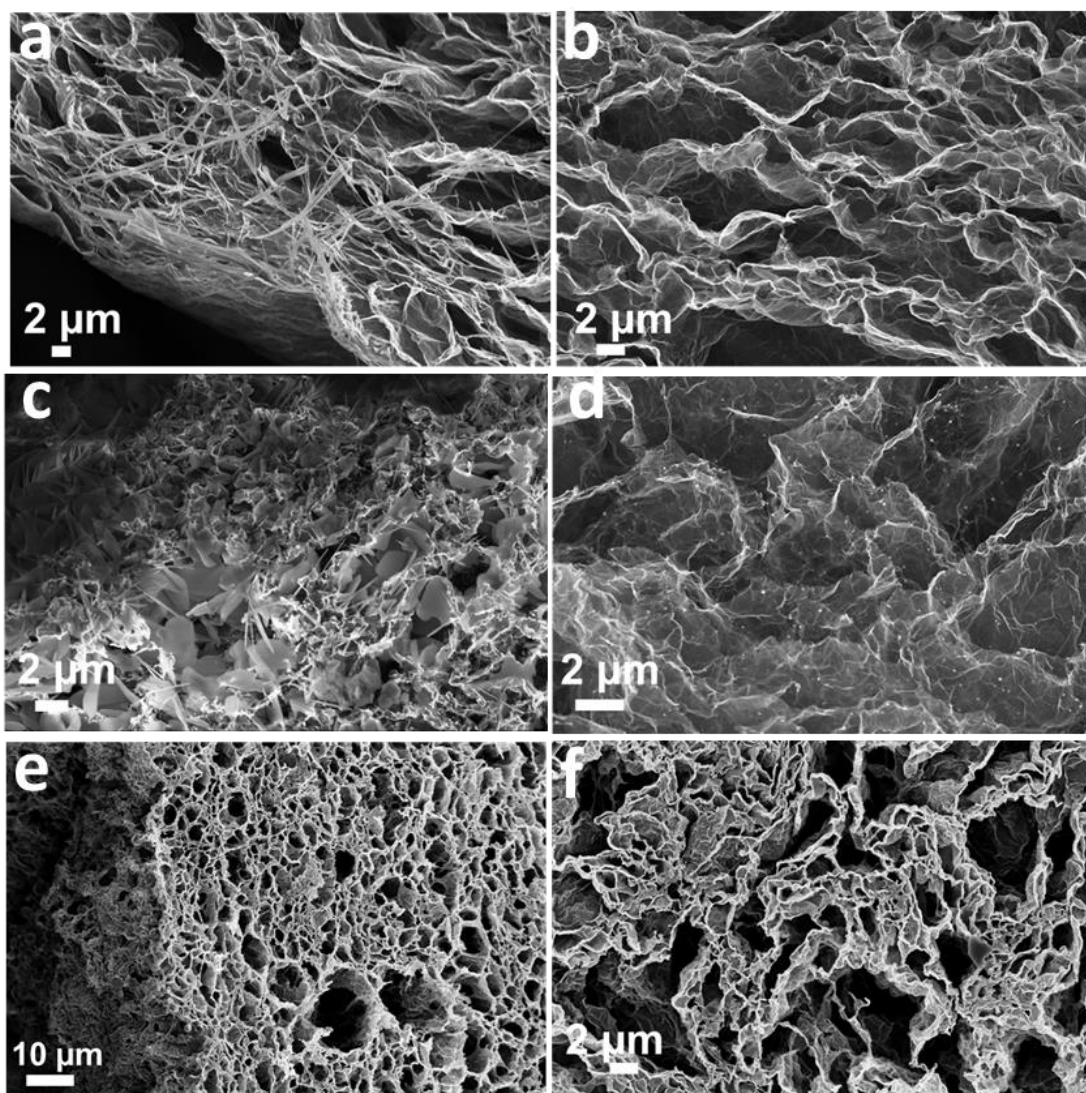
Fig. S13: XRD study of MOFs prepared at different concentrations of reactants: (a) AOGZIF67-PG, (b) AOGCu(BTC)-PG, (c) AOGTM-PG[R] and (d) AOGTM-PG[S].
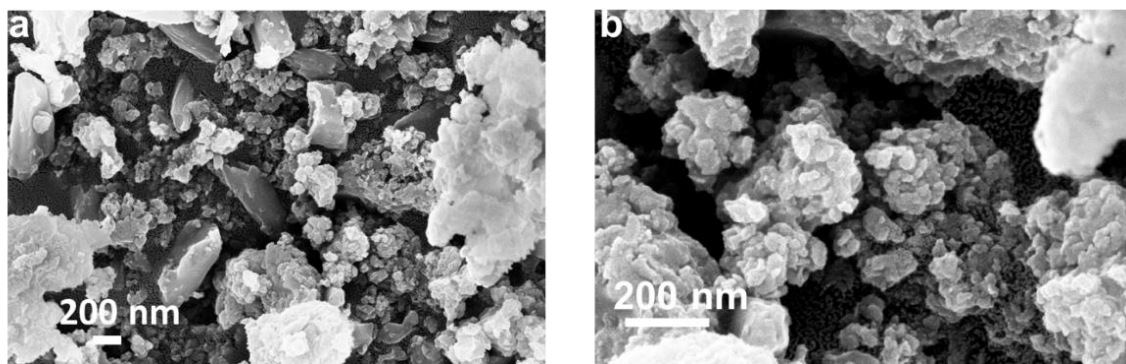
Fig. S14: (a)-(b) FE-SEM images of non-uniform particles of $_{AO}$TM[S] (synthesized by bulk interfacial reaction) at different magnifications.
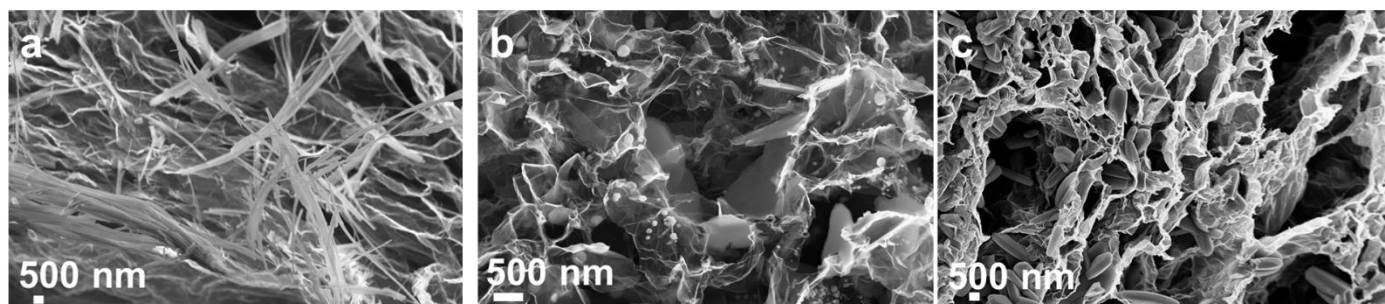
Fig. S15: FE-SEM images of water phase synthesis of MOFs within PG: (a) $_{AG}$Cu(BTC)-PG, (b) $_{AG}$ZIF67-PG and (c) $_{AG}$ZIF8-PG.

Fig. S16: Surface confined water phase synthesis of (a)-(b) $_{AG}$Cu(BTC)-PG, (c)-(d) $_{AG}$ZIF67-PG and (e)-(f) $_{AG}$ZIF8-PG. Figure (a), (c) and (e) show the growth of MOFs just below the outer surface of PG and Figure (b), (d) and (f) show that the concentration of as grown MOFs decrease in the interior of the PG.
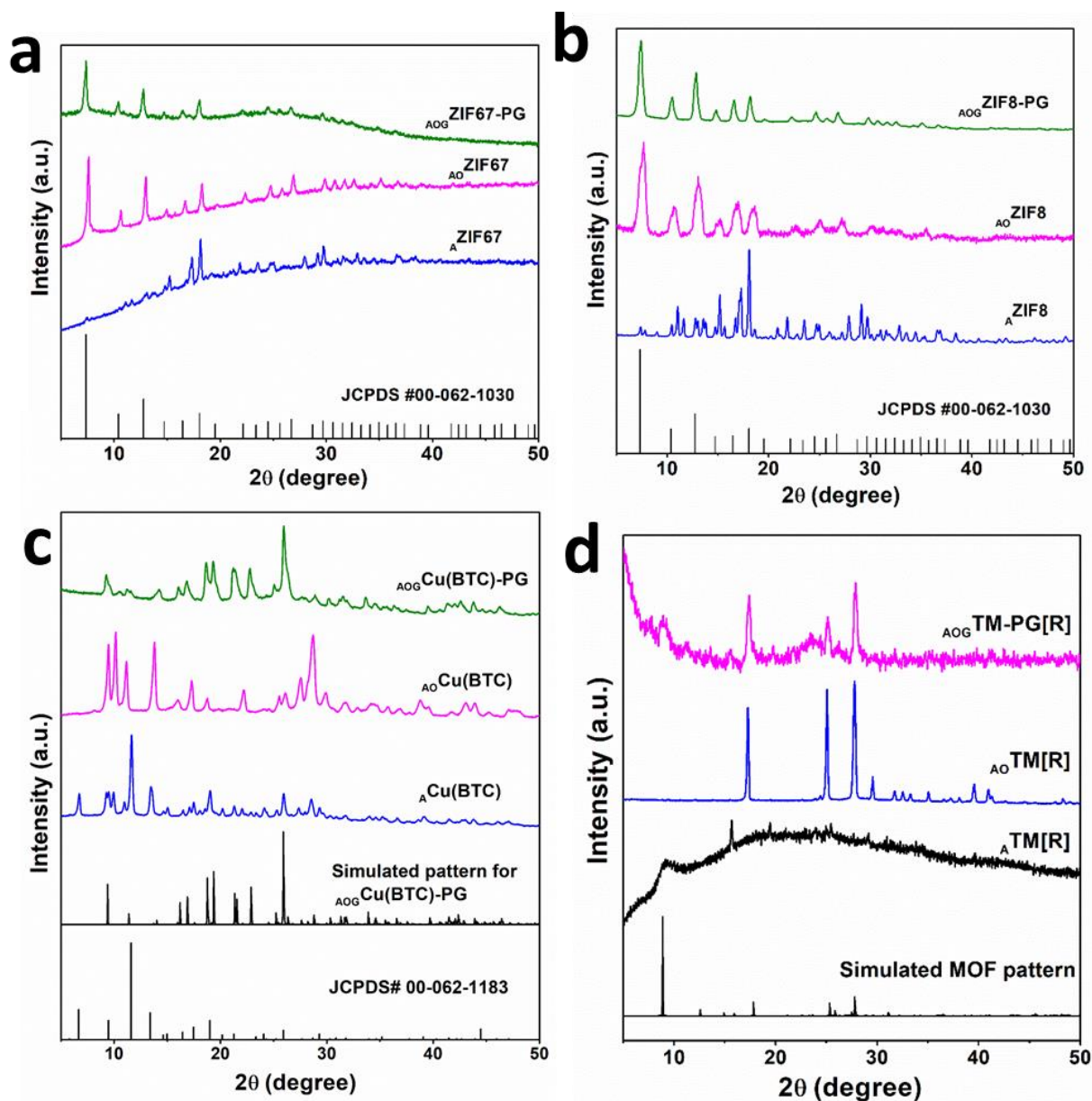
Fig. S17: Comparison of XRD patterns of various MOFs and MOF-PG hybrids synthesized by different methods: (a) AOGZIF67-PG, AOZIF67 and AZIF67; (b) AOGZIF8-PG, AOZIF8 and AZIF8; (c) AOGCu(BTC)-PG, AOCu(BTC) and ACu(BTC) and (d) AOGTM-PG[R], AOTM[R] and ATM[R].
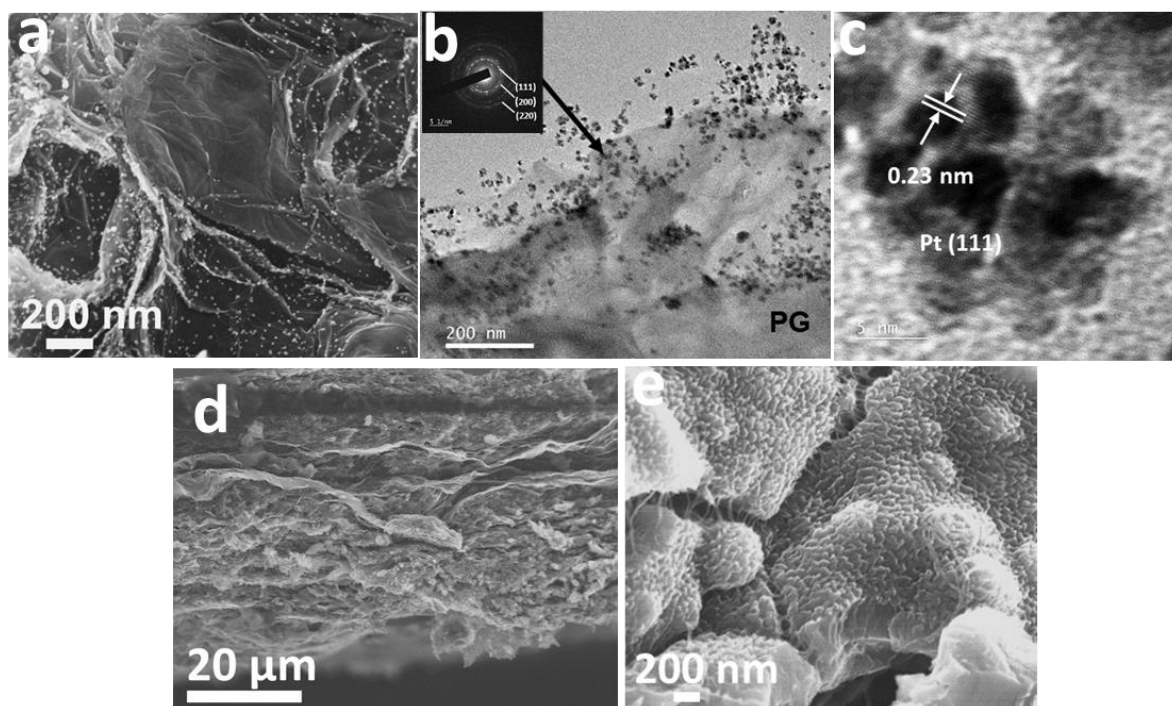
Fig. S18: FE-SEM images of (a) AOGPt-PG, (d)-(e) AOGPANI-PG (at different magnifications); (b) FE-TEM and (c) HR-TEM images of AOGPt-PG; inset of (b) shows the corresponding SAED pattern.
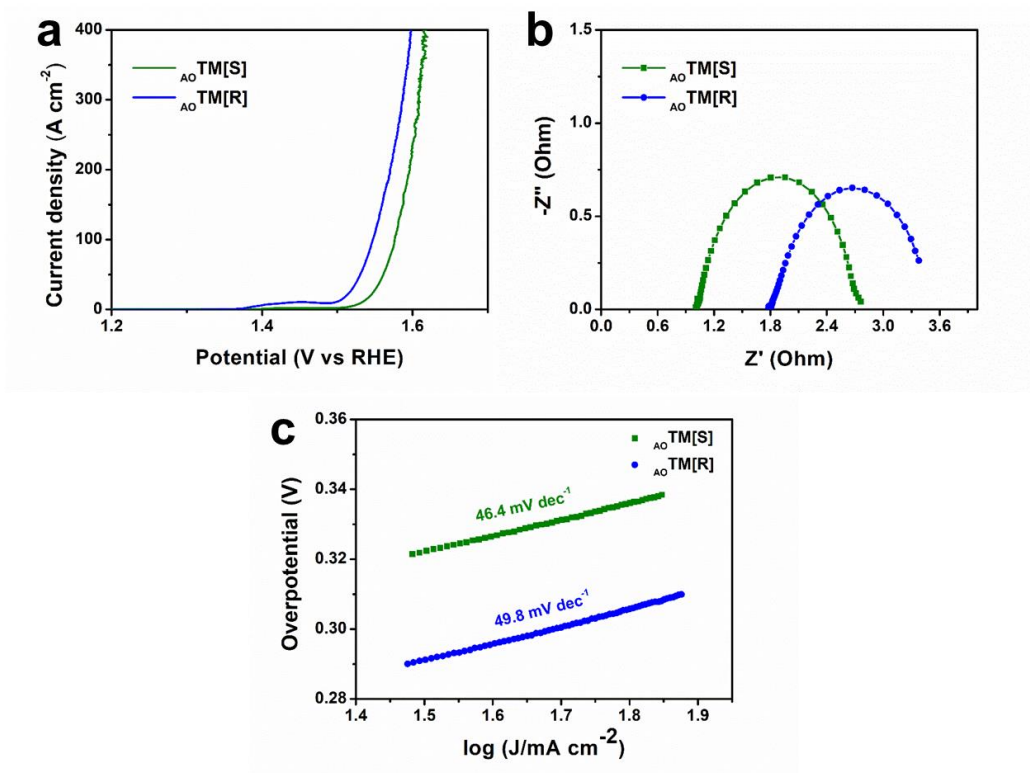
Fig. S19: Electrochemical characterization of bulk MOFs: (a) LSV plot, (b) EIS spectra and (c) Tafel plots of $_{AO}$TM[R] and $_{AO}$TM[S].
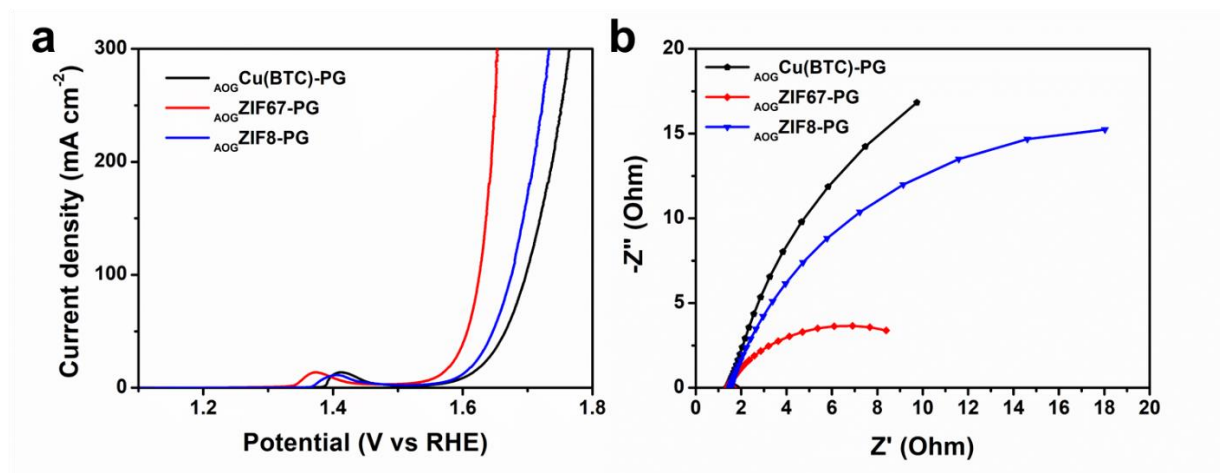
Fig S20: (a) LSV plots and (b) EIS spectra of $_{AOG}$ZIF67-PG, $_{AOG}$ZIF8-PG and $_{AOG}$Cu(BTC)-PG.
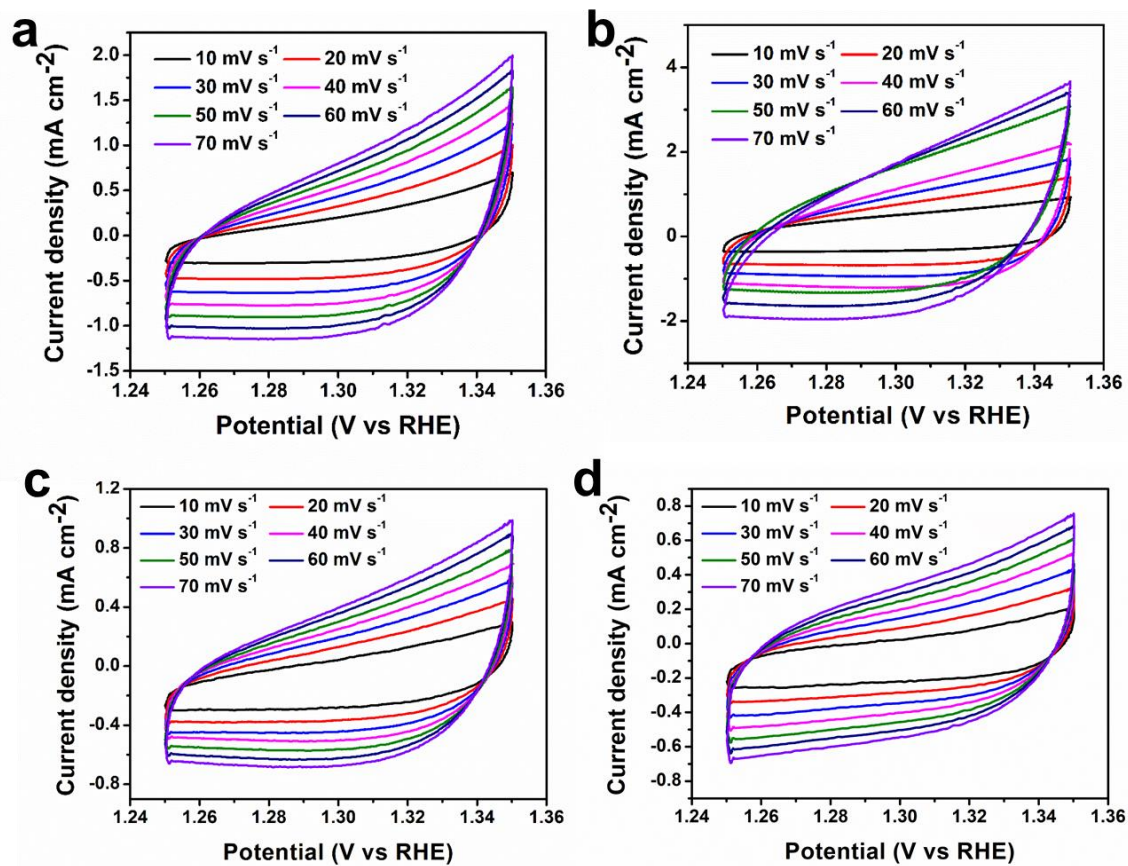
Fig. S21: Cyclic voltammetry curves of (a) AOGTM-PG[R], (b) AOGTM-PG[S], (c) AOTM[R] and (d) AOTM[S] in the non-Faradaic region.
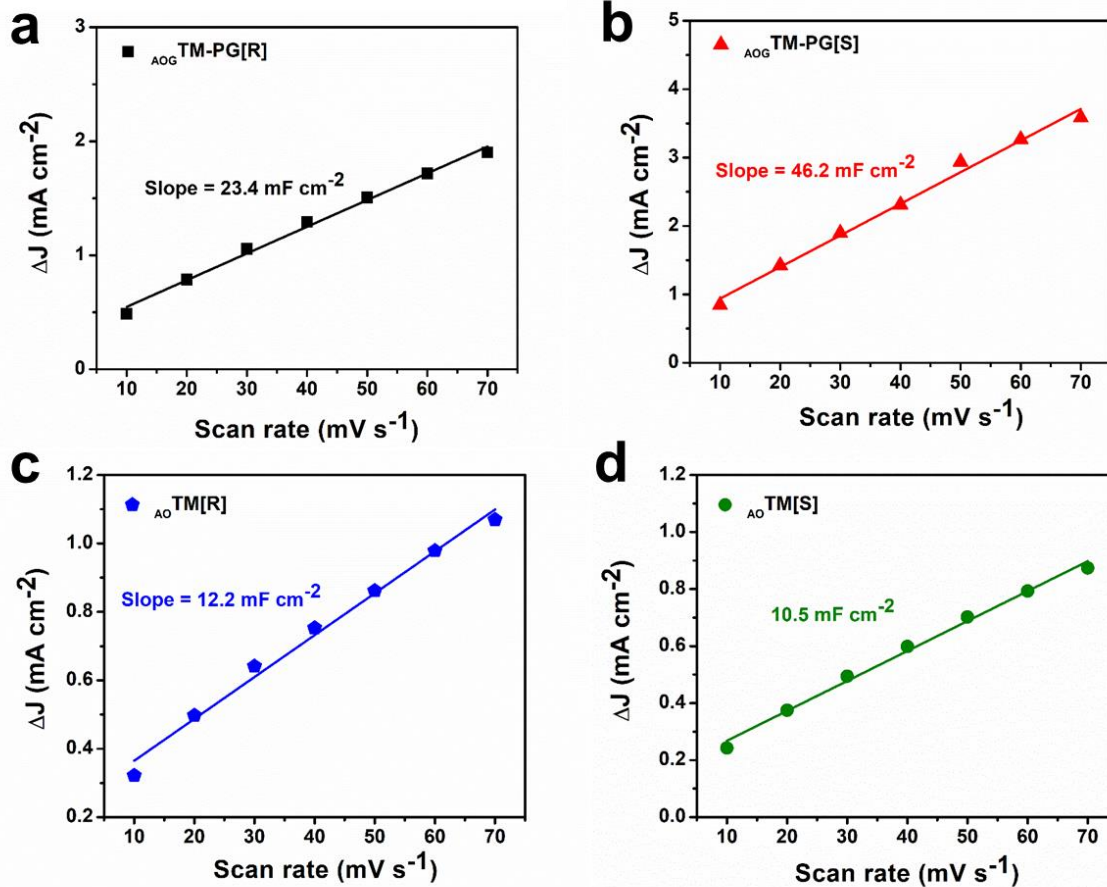
Fig. S22: Linear plots of $\Delta J = (J_a - J_c)$ vs scan rates for (a) AOGTM-PG[R], (b) AOGTM-PG[S], (c) AOTM[R] and (d) AOTM[S].
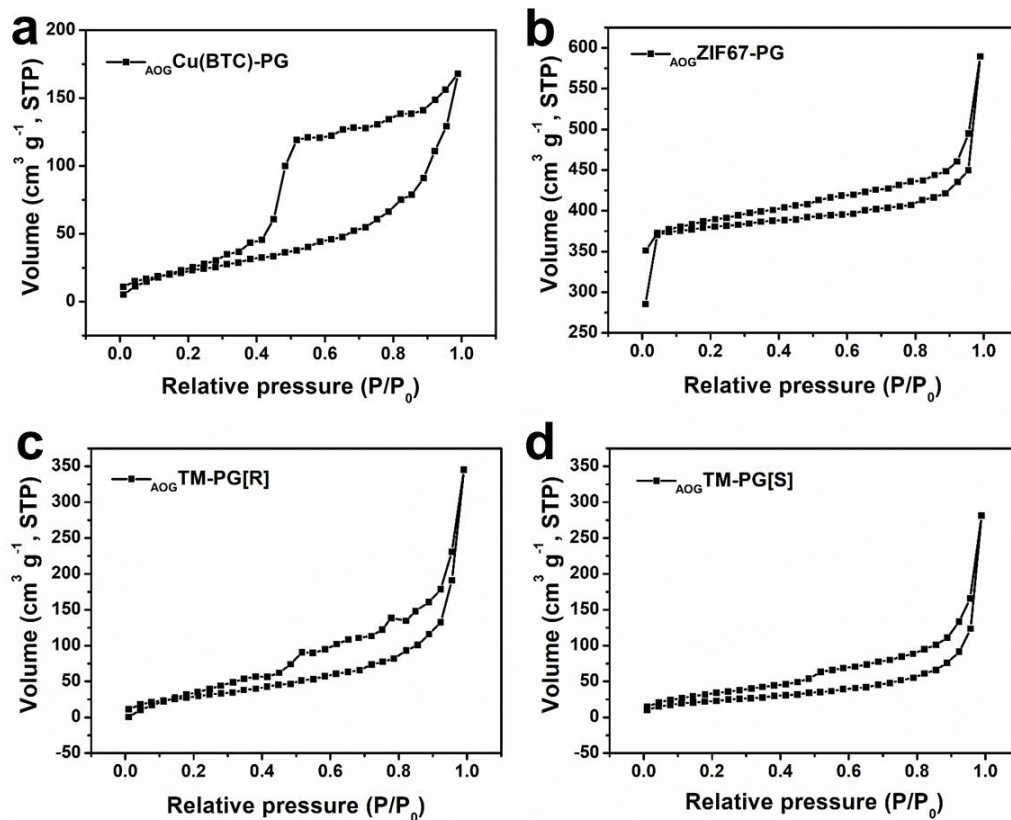
Fig. S23: N$_2$ adsorption/desorption isotherms for (a) $_{AOG}$Cu(BTC)-PG, (b) $_{AOG}$ZIF67-PG, (c) $_{AOG}$TM-PG[R] and (d) $_{AOG}$TM-PG[S].

Table S4: BET specific surface area of MOF-PG hybrids

	$_{AOG}$ZIF67-PG	$_{AOG}$Cu(BTC)-PG	$_{AOG}$TM-PG[R]	$_{AOG}$TM-PG[S]
BET specific surface area (m^2 g^{-1})	1105	85.9	111	83
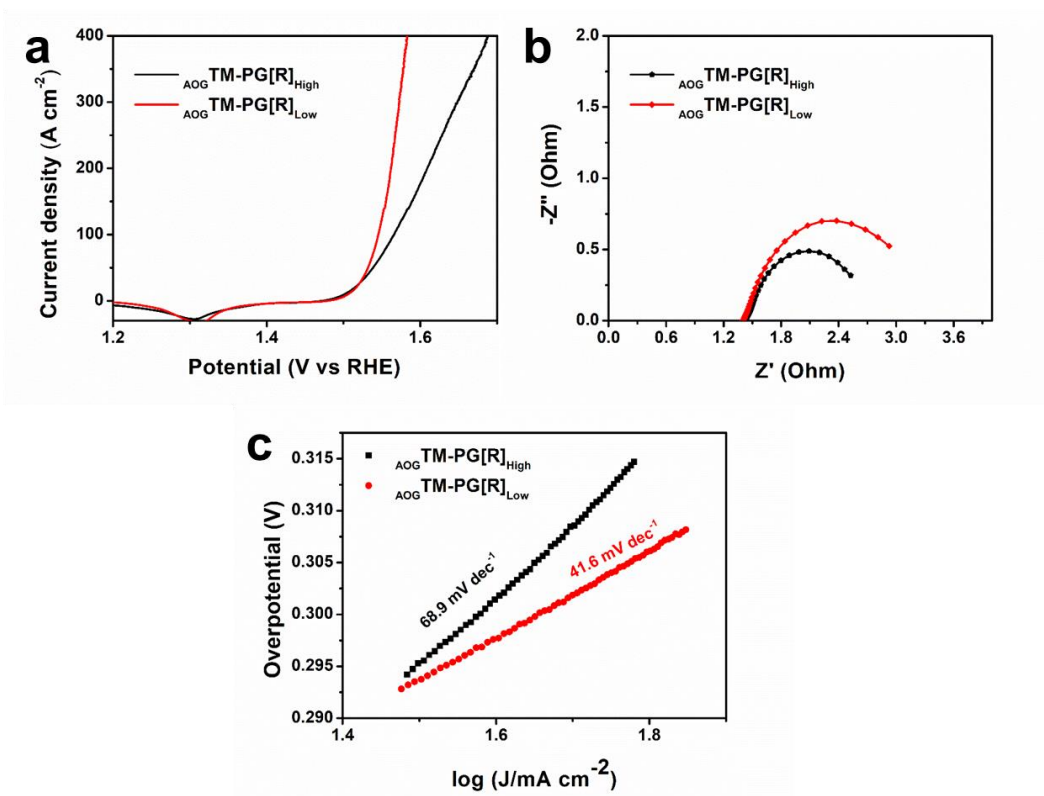
Fig. S24: (a) LSV plot, (b) EIS spectra and (c) Tafel plots of ₐₒGTM-PG[R] prepared at different reactant concentrations.
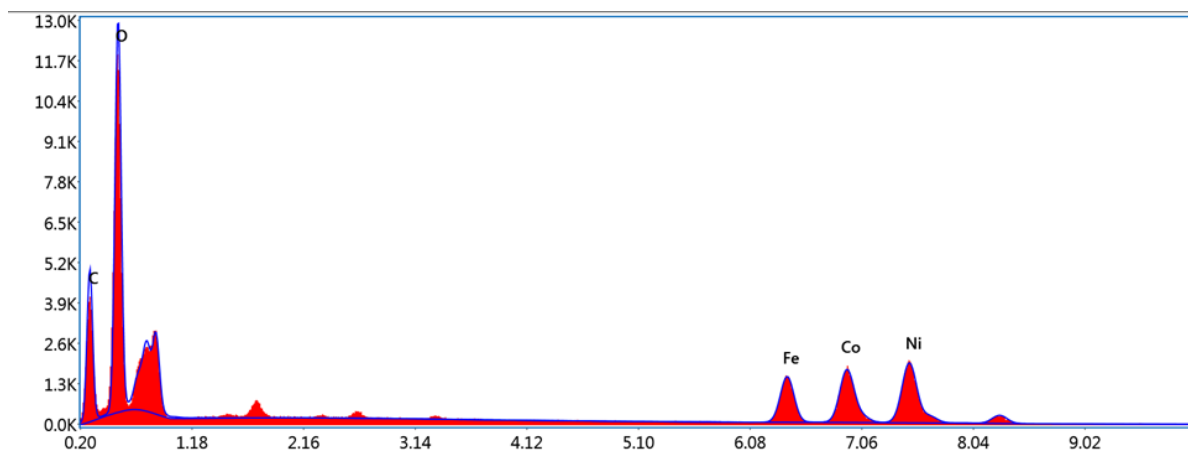
Element	Weight %	Atomic %	Error %	Net Int.	K Ratio	Z	A	F
C K	22.18	39.69	8.50	1024.62	0.0762	1.1347	0.3028	1.0000
O K	32.38	43.50	7.76	2897.59	0.1247	1.0895	0.3535	1.0000
Fe K	10.25	3.95	3.19	738.12	0.0962	0.8449	1.0095	1.1005
Co K	15.03	5.48	2.85	876.79	0.1300	0.8257	1.0087	1.0380
Ni K	20.16	7.38	2.51	1033.34	0.1736	0.8536	0.9979	1.0111

Fig. S25: EDAX elemental analysis of $_{AOG}$TM-PG[R] after OER cycling.

Table S5: Comparison of electrocatalytic OER performances of existing MOF based and transition metal double hydroxide based water oxidation catalysts

Nature of catalyst	Catalyst	Mass loading (mg cm^{-2})	Electrolyte	Overpotential at		Tafel slope (mV dec^{-1})	Ref
				10 mA cm^{-2} (mV)	100 mA cm^{-2} (mV)		
MOF based catalysts	$_{AOG}$**TM-PG[R]**	**0.64**	**1M KOH**	**255**	**300**	**44.3**	**This work**
	(Ni$_2$Co$_1$)$_{0.925}$Fe$_{0.075}$-MOF	0.54	1M KOH	257	312	41.3	14
	Co$_2$(μ-OH)$_2$(bbta) (MAFX27-OH)	1.13	1M KOH	292	-	88	15
	Co-ZIF-9	0.2	Potassium phosphate+KOH (pH= 13.4)	510 at 1 mA cm^{-2}	-	93	16
	CUMS-ZIF67	0.1	0.5 M KBi (pH = 9.2)	410	-	185.1	17
	PANI-ZIF67	0.6	1M KOH	330	-	37	18
	Ni-MOF@FeMOF	0.2	1M KOH	265	-	82	19
	Ti$_3$C$_2$T$_x$–CoBDC	0.21	0.1M KOH	410	-	48.2	20
	CoOx-ZIF	0.2	1M KOH	318	-	70.3	21
	3D Graphene/Ni-MOF	0.29	0.1M KOH	370	-	91	22
	2D CoZIF-9(III) sheets	0.21	1M KOH	380	-	55	23
	EG/Co(OH)2/ZIF-67		1M KOH	280		63	24
Other transition metal based catalysts	NiV	0.143	1M KOH	300	-	50	25
	NiFe LDH nanosheet	1	1M KOH	302	-	40	26
	Fe-Co LDH	0.21	1M KOH	323	-	85	27
	Ni-Fe LDH hollow nanoprisms	0.16	1M KOH	280	339	49.4	28
	MOF derived Co$_3$N@AN-C NCs	2.6	1M KOH	280	-	69.6	29
	Ni$_{0.7}$Fe$_{0.3}$@Ni$_{0.7}$Fe$_{0.3}$O/NF	2	1M KOH	215	260	47.4	30

References:

1. U.N. Maiti, J. Lim, K.E. Lee, W.J. Lee, S.O. Kim, *Adv. Mater.* 2014. **26**: p. 615-619.

2. X. Wang, F. Wan, L. Zhang, Z. Zhao, Z. Niu, J. Chen, Adv. Funct. Mater. 2018. **28**: p. 1707247.

3. J. Huang and R.B. Kaner, *J. Am. Chem. Soc.* 2004. **126**(3): p. 851-855.

4. M. D. Hanwell, D.E. Curtis, D.C. Lonie, T. Vandermeersch, E. Zurek, G.R. Hutchison, *J. Cheminformatics* 2012. **4**(1): p. 17.

5. W. Humphrey, A. Dalke, and K. Schulten, *J. Mol. Graph.* 1996. **14**(1): p. 33-38.

6. H. Tang, D. Liu, Y. Zhao, X. Yang, J. Lu, F. Cui, *J. Phys. Chem. C*, 2015. **119**(47): p. 26712-26718.

7. J. C. Phillips, R. Braun, W. Wang, J. Gumbart, E. Tajkhorshid, E. Villa, C. Chipot, R.D. Skeel, L. Kalé, K. Schulten, *J. Comput. Chem*, 2005. **26**(16): p. 1781-1802.

8. W. L. Jorgensen, D.S. Maxwell, and J. Tirado-Rives, *J. Am. Chem. Soc.* 1996. **118**(45): p. 11225-11236.

9. W. L. Jorgensen, J. Chandrasekhar, J.D. Madura, R.W. Impey, M.L. Klein, *J. Chem. Phys.* 1983. **79**(2): p. 926-935.

10. S. Miyamoto and P.A. Kollman, *J. Comput. Chem*, 1992. **13**(8): p. 952-962.

11. U. Essmann, L. Perera, M.L. Berkowitz, T. Darden, H. Lee, L.G. Pedersen, *J. Chem. Phys.* 1995. **103**(19): p. 8577-8593.

12. A. Kojtari, P.J. Carroll, H.-F. Ji, CrystEngComm. 16(2014) 2885-2888.

13. A. Mesbah, P. Rabu, R. Sibille, S. Lebegue, T. Mazet, B. Malaman, M. Francois, *Inorg. Chem.* 2014, **53**(2): p. 872-871.

14. Q. Qian, Y. Li, Y. Liu, L. Yu and G. Zhang, *Adv. Mater.* 2019, **31**: p.1901139.

15. X. F. Lu, P. Q. Liao, J. W. Wang, J. X. Wu, X. W. Chen, C. T. He, J. P. Zhang, G. R. Li, X. M. Chen, *J. Am. Chem. Soc.* 2016. **138**(27): p. 8336-8339.

16. S. Wang, Y. Hou, S. Lina, X. Wang, *Nanoscale*, 2014. **6**(17): p. 9930-9934.

17. L. Tao, C. Y. Lin, S. Dou, S. Feng, D. Chen, D. Liu, J. Huo, Z. Xia, S. Wang, *Nano Energy*, 2017. **41**: p. 417-425.

18. M. Khalid, A. M. B. Honorato, H. Varela, L. Dai, *Nano Energy*, 2018. **45**: p. 127-135.

19. K. Rui G. Zhao, Y. Chen, Y. Lin, Q. Zhou, J. Chen, J. Zhu, W. Sun, W. Huang, S. X. Dou, *Adv. Funct. Mater.* 2018. **28**(26): p. 1801554.

20.   L. Zhao, B. Dong, S. Li, L. Zhou, L. Lai, Z. Wang, S. Zhao, M. Han, K. Gao, M. Lu, X. Xie, B. Chen, Z. Liu, X. Wang, H. Zhang, H. Li, J. Liu, H. Zhang, X. Huang, W. Huang. *ACS Nano.* 2017, **11**(6): p. 5800-5807.

21.   S Dou, CL Dong, Z Hu, YC Huang, J Chen, L Tao, D. Yan, D. Chen, S. Shen, S. Chou, S. Wang, *Adv. Funct. Mater.* 2017. **27**(36): p. 1702546.

22.   A. Xie, J. Du, F. Tao, Y. Tao, Z. Xiong, S. Luo, X. Li, C. Yao, *Electrochim. Acta*, 2019. **305** p. 338e348.

23.   K. Jayaramulu, J. Masa, D. M. Morales, O. Tomanec, V. Ranc, M. Petr, P. Wilde, Y. – T. Chen, R. Zboril, W. Schuhmann and R. A. Fischer, *Adv. Sci.* 2018. **5**: p. 1801029.

24.   J. Cao, C. Lei, J. Yang, X. Cheng, Z. Li, B. Yang, X. Zhang, L. Lei, Y. Hou, K. Ostrikov, *J. Mater. Chem. A*, 2018. **6**: p. 18877-18883.

25.   K. Fan, H. Chen, Y. Ji, H. Huang, P. M. Claesson, Q. Daniel, B. Philippe, H. Rensmo, F. Li, Y. Luo, L. Sun, *Nat. Commun.* 2016. **7**: p. 11981.

26.   F. Song and X. Hu, *Nat. Commun.* 2014. **5**: p. 4477.

27.   B. Zhang, X. Zheng, O. Voznyy1, R. Comin, M. Bajdich, M. G. Melchor, L. Han, J. Xu, M. Liu, L. Zheng, F. P. G. D. Arquer, C. T. Dinh, F. Fan, M. Yuan, E. Yassitepe, N. Chen, T. Regier, P. Liu, Y. Li, P. D. Luna, A. Janmohamed, H. L. Xin, H. Yang, A. Vojvodic, E. H. Sargent, *Science*, 2016. **352**(6283): p. 333.

28.   L. Yu, J. F. Yang, B. Y. Guan, Y. Lu, X. W. Lou, *Angew. Chem.* 2018. **57**(1): p. 172-176.

29.   B. K. Kang, S. Y. Im, J. Lee, S. H. Kwag, S. B. Kwon, S. N. Tiruneh, M-J. Kim, J. H. Kim, W. S. Yang, B. Lim, D. H. Yoon, *Nano Res*. 2019. **12**, p. 1605–1611.

30.   Z. Yang, X. Liang, *Nano Res*. 2020. **13**, p. 461-466